Acta Crystallographica Section A
Foundations of Crystallography
ISSN 0108-7673

Received 20 July 2009
Accepted 6 February 2010

Electron beam–specimen interactions and their effect on high-angle annular dark-field imaging of dopant atoms within a crystal

B. G. Mendis

Department of Physics, Durham University, South Road, Durham DH1 3LE, UK. Correspondence e-mail: b.g.mendis@durham.ac.uk

A Bloch wave model based on perturbation theory is used to analyse high-angle annular dark-field (HAADF) imaging of a substitutional and interstitial W atom in [111]-oriented body-centred-cubic Fe. For the substitutional atom the 1*s* Bloch state is scattered to high angles thereby producing HAADF dopant atom contrast. Intraband scattering of the 1*s* state is the strongest individual Bloch wave transition but collective interband scattering of the non-1*s* states to the 1*s* state leads to variations in the high-angle scattering with depth of the dopant atom. The non-1*s* states are Coulomb attracted towards the W atom thereby giving rise to an 'atom focusing' effect similar to channelling. For the interstitial atom, which in the [111] orientation does not overlap with an atom column of the host lattice, high-angle scattering and Coulomb attraction takes place through the non-1*s* states. Scattering of the 1*s* state is, however, negligible.

1. Introduction

Imaging individual dopant atoms is finding increasing application in semiconductor (Voyles *et al.*, 2002, 2003, 2004; van Benthem *et al.*, 2005; Allen *et al.*, 2008) and catalysis (Nellist & Pennycook, 1996; Shannon *et al.*, 2007) research. High-angle annular dark-field (HAADF) imaging in scanning transmission electron microscopy (STEM) has proved to be highly successful in detecting dopant atoms. The HAADF signal consists of the electron intensity scattered to large angles that is collected by a post-specimen annular detector. The scattering is due to interaction of the incident electrons with the nucleus of the scattering atom, *i.e.* Rutherford scattering (Pennycook & Jesson, 1991). HAADF images therefore show strong atomic number contrast. Furthermore, unlike phase contrast images, HAADF is an incoherent imaging technique so that the image can be directly interpreted up to the resolution limit. This can be expressed mathematically as (Pennycook & Jesson, 1991; Cosgriff & Nellist, 2007)

$$I_{\mathrm{HAADF}} = \sum \sigma_{\mathrm{HA}} |\Psi|^2 \tag{1}$$

where I_{HAADF} is the HAADF intensity and $|\Psi|^2$ is the square modulus of the electron wavefunction (*i.e.* electron beam intensity) at the position of the scattering atom of high-angle-scattering cross section σ_{HA}. The summation is carried out over all atoms within the electron beam path. If a crystal contains a dopant atom then a change in I_{HAADF} occurs owing to a change in σ_{HA}. However, the change in HAADF intensity also depends on the local electron beam intensity and hence the contrast of a dopant atom is expected to vary with its depth within the specimen (Voyles *et al.*, 2004).

Owing to the periodic potential of the lattice an incident electron plane wave will set up standing waves, called Bloch waves, within a crystal (Hirsch *et al.*, 1965). One such Bloch wave, called the 1*s* state, channels along the atom columns (Buxton *et al.*, 1978). Nellist & Pennycook (1999) have shown theoretically that the annular detector used in HAADF imaging acts as a filter for the 1*s* Bloch state. In a defect crystal, such as a crystal containing a dopant atom, the excitation of individual Bloch waves undergoes change owing to additional scattering mechanisms that depend on the nature of the defect. Scattering in the presence of slowly varying elastic strain fields is described by the Howie–Whelan equations (Hirsch *et al.*, 1965). However, the Howie–Whelan equations cannot be applied to a dopant atom where the scattering is largely due to a change in the local electrostatic potential and is hence chemical in nature. The author of this paper has applied time-dependent perturbation theory to analyse electron beam scattering owing to a dopant atom (Mendis, 2008). In this paper perturbation theory is used to analyse dopant atom scattering and its effect on the HAADF image. A detailed understanding of the fundamental physics of image formation could provide insight into novel methods for improving HAADF dopant atom contrast as well as establishing the intrinsic limits of optical sectioning experiments in aberration-corrected scanning transmission electron microscopes (van Benthem *et al.*, 2005; Allen *et al.*, 2008).

In §2 of this paper the perturbation method and computational procedure for STEM imaging is described. W substitutional and interstitial atoms in a [111]-oriented Fe crystal are investigated as a model system. The Fe–W system was selected on the basis that it is a relatively simple crystal for carrying out

doi:10.1107/S0108767310004770

Bloch wave analyses on dopant atom scattering. This paper does not present results for the more commonly studied materials, such as semiconductors or perovskites, but it is expected that the analysis of these systems would proceed along similar lines to the methods developed for Fe–W. In §3 the simulation results are presented and discussed. Results from the Bloch wave perturbation theory are compared with multislice simulations (Cowley & Moodie, 1957; Kirkland, 1998) to confirm their validity. A summary and conclusions are presented in §4.

2. Perturbation theory and STEM calculation procedure

When a dopant atom is placed in an otherwise perfect crystal the electrostatic potential is perturbed locally (in this paper we shall neglect the strain field surrounding the dopant atom). An excess potential υ is introduced at the site of the dopant atom. For a substitutional atom, υ is equal to the difference in potential between the dopant atom and host atom while for an interstitial atom it is equal to the dopant atom potential. If the excess potential is small then the wave profile of the Bloch states remains largely unchanged compared with a perfect crystal. However, the excitation of individual Bloch states can change owing to scattering by the dopant atom. Since high-energy electrons have short wavelengths, dopant atom scattering takes place within a narrow column of material centred about the dopant atom and extending through the thickness of the specimen. This is the so-called column approximation (Hirsch *et al.*, 1965). Columns not containing the dopant atom do not produce any change to the Bloch state excitations and hence electron beam propagation is identical to that of a perfect crystal. Time-dependent perturbation theory can be applied to calculate the change in Bloch state excitations ε as a function of the depth z within the column containing the dopant atom (Mendis, 2008). The result for an incident high-energy electron plane wave is expressed as (Mendis, 2008)

$$\frac{\mathrm{d}\varepsilon^{q}(\mathbf{k}_{\rm t}, z)}{\mathrm{d}z} = \frac{2\pi i m e}{h^{2}k_{z}} \sum_{p} \varepsilon^{p}(\mathbf{k}_{\rm t}, z) \exp[2\pi i(\gamma^{p} - \gamma^{q})z] \times \int b^{p}(\mathbf{k}_{\rm t}, \mathbf{R}) \upsilon(\mathbf{R}, z) b^{q}(\mathbf{k}_{\rm t}, \mathbf{R})^{*} \, \mathrm{d}\mathbf{R}, \qquad (2)$$

where m and e are the relativistic mass and charge of an electron, h is Planck's constant and k_z is the magnitude of the longitudinal component of the incident electron wavevector parallel to the optic (*i.e.* z) axis. γ is the change in longitudinal wavevector for a given Bloch state due to channelling. The superscripts p and q represent individual Bloch state indices and the asterisk symbol (*) is used to denote the complex conjugate. The summation in (2) is carried out over all Bloch states. Furthermore,

$$b^{q}(\mathbf{k}_{\rm t}, \mathbf{R}) = \sum_{\mathbf{g}} C_{\mathbf{g}}^{(q)}(\mathbf{k}_{\rm t}) \exp\big[2\pi i(\mathbf{k}_{\rm t} + \mathbf{g}) \cdot \mathbf{R}\big], \qquad (3)$$

where $C_{\mathbf{g}}^{(q)}(\mathbf{k}_{\rm t})$ are Fourier components of the qth Bloch state in a *perfect* crystal, $\mathbf{k}_{\rm t}$ is the transverse wavevector of the incident electron and $\mathbf{R}$ denotes a two-dimensional position vector. Both $\mathbf{k}_{\rm t}$ and $\mathbf{R}$ lie in the plane normal to the optic axis. The summation in (3) is carried out over all reciprocal-lattice vectors $\mathbf{g}$ in the zero-order Laue zone (ZOLZ) plane. The restriction on $\mathbf{g}$ is due to neglecting high-order Laue zone (HOLZ) reflections in the derivation of (2) (Mendis, 2008).

The STEM objective aperture contains many different wavevectors that collectively form the incident electron probe. Each wavevector will excite several Bloch states within the specimen such that the boundary conditions are satisfied, *i.e.* at the specimen entrance surface the unscattered beam has a normalized intensity of 1 and the diffracted beams have zero intensity (Hirsch *et al.*, 1965). The STEM electron wavefunction, $\Psi(\mathbf{R}, z)$, within the specimen is given by (Pennycook & Jesson, 1991; Cosgriff & Nellist, 2007)

$$\Psi(\mathbf{R}, z) = \sum_{q} \int \varepsilon^{q}(\mathbf{k}_{\rm t}, z) b^{q}(\mathbf{k}_{\rm t}, \mathbf{R}) \exp\big[2\pi i\big(k_{z} + \gamma^{q}\big)z\big] \times \exp(-2\pi i \mathbf{k}_{\rm t} \cdot \mathbf{R}_{\rm o}) \, \mathrm{d}\mathbf{k}_{\rm t}, \qquad (4)$$

where $\mathbf{R}_{\rm o}$ is the two-dimensional position vector of the incident electron probe. Integration is carried out over all transverse wavevectors $\mathbf{k}_{\rm t}$ within the objective aperture. In (4) it is assumed that all electron optic aberrations are zero.

Equations (2)–(4) provide a method for calculating STEM probe propagation within the narrow column containing the dopant atom. For a given incident wavevector within the objective aperture the excitations and wave profiles of the Bloch states are first calculated as would be carried out for a perfect crystal. The specimen is divided into thin slices along the z axis in the vicinity of the dopant atom. The change in excitation owing to dopant atom scattering as the beam propagates through a thin slice is calculated using equation (2). This calculation is repeated for each incident wavevector within the STEM probe. The new excitation values for each incident wavevector can then be substituted into (4) to determine the STEM electron wavefunction at a given depth in the defect crystal. Note that the slice method and (2) need only be applied at depths where the excess potential υ is non-zero.

The potential of an atom is calculated by inverse Fourier transforming its atom scattering factor (Kirkland, 1998; Mendis, 2008) and from this the excess potential υ is derived. The atomic potential calculated using the above method is a real number. For accurate simulation of HAADF images it is necessary to include the specimen thermal diffuse scattering (TDS). In the multislice method TDS is taken into account using the frozen phonon technique (Loane *et al.*, 1988; Kirkland, 1998). In the Bloch wave method TDS is modelled phenomenologically by adding an imaginary term to the atomic potential or equivalently the atom scattering factor (Hirsch *et al.*, 1965). The imaginary part of the atom scattering factor is called the absorption form factor (Hall & Hirsch, 1964; Bird & King, 1990) and its inverse Fourier transform gives the imaginary part of the atom potential. The excess potential υ in (2) is therefore a complex number.

Electron beam scattering by substitutional and interstitial W atoms in a [111]-oriented 100 Å-thick body-centred-cubic (b.c.c.) Fe crystal was investigated using the above simulation procedure. The interstitial atom was placed at the octahedral interstice of the b.c.c. lattice (Fig. 1*a*). The interstitial does not overlap with any atom columns of the host lattice when viewed along the [111] orientation (Fig. 1*b*). The microscope acceleration voltage was 300 kV and the STEM probe semi-convergence angle was 20 mrad. 121 Bloch states were calculated for each of the 484 wavevectors within the STEM probe. The atom scattering factors of Kirkland (1998) and Debye–Waller factors of Gao & Peng (1999) were used in the simulations. When applying (2) the specimen was divided into 0.1 Å-thick slices within a depth of 1 Å either side of the dopant atom. It is emphasized that the Bloch wave calculations are only approximate since the perturbation theory is only valid for small excess potentials; this condition is not strictly satisfied in the Fe–W system, which has an atom number difference of 48. Hence multislice frozen phonon simulations, using the code developed by Kirkland (1998), were also carried out to ensure that the Bloch wave results were, however, qualitatively correct. 20 to 40 frozen phonon configurations were averaged for each simulation condition. The lateral dimensions of the supercell was 18.7 × 20.2 Å with the dopant atom placed in approximately the centre. 512 × 512 image pixels were used to sample the projected potential. Slicing of the supercell was based on the *ABC* stacking sequence for a perfect [111]-b.c.c. crystal and consequently the slice thickness was 0.8 Å. The HAADF detector had an inner angle of 100 mrad and an outer angle of 200 mrad.

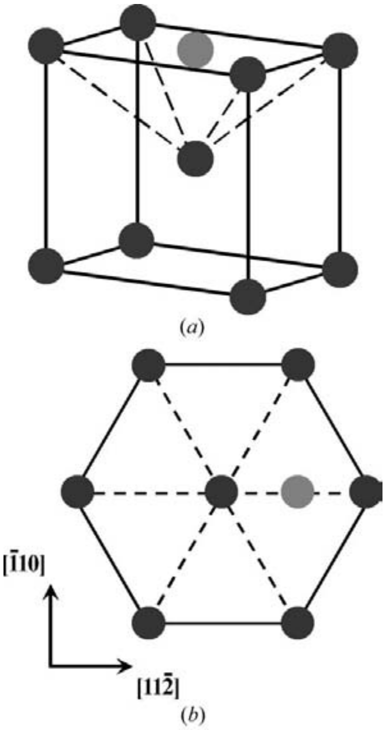

Figure 1
(*a*) Schematic showing an interstitial atom placed in the octahedral interstice of a b.c.c. crystal. The interstitial atom is in grey while the host atoms are darker in colour. The octahedral interstice is outlined by the dashed lines (only one half of the interstice is shown). In (*b*) the position of the octahedral interstitial atom when the crystal is viewed along the [111] projection is shown.

3. Results and discussion

3.1. STEM probe *Pendellösung* for substitutional W in [111]-Fe

In this section the STEM probe *Pendellösung* will be analysed within the column containing the dopant atom. First, however, it is necessary to establish the validity of the column approximation for the simulation conditions used in this paper. A purely geometric argument suggests that for a STEM probe semi-convergence angle ($\alpha_{\rm probe}$) of 20 mrad the beam radius at the exit surface of a foil with thickness (t) 100 Å should be approximately $\alpha_{\rm probe}t$ or 2 Å. This is a similar dimension to the inter-columnar spacing of 2.3 Å for [111]-Fe. In practice, beam spreading will be reduced for a probe positioned over an atom column owing to channelling in thin foils (Fertig & Rose, 1981). Fig. 2(*a*) shows the square modulus of the exit wavefunction for an aberration-free 20 mrad STEM probe positioned over an atom column in a 100 Å-thick perfect [111]-Fe specimen determined by multislice frozen

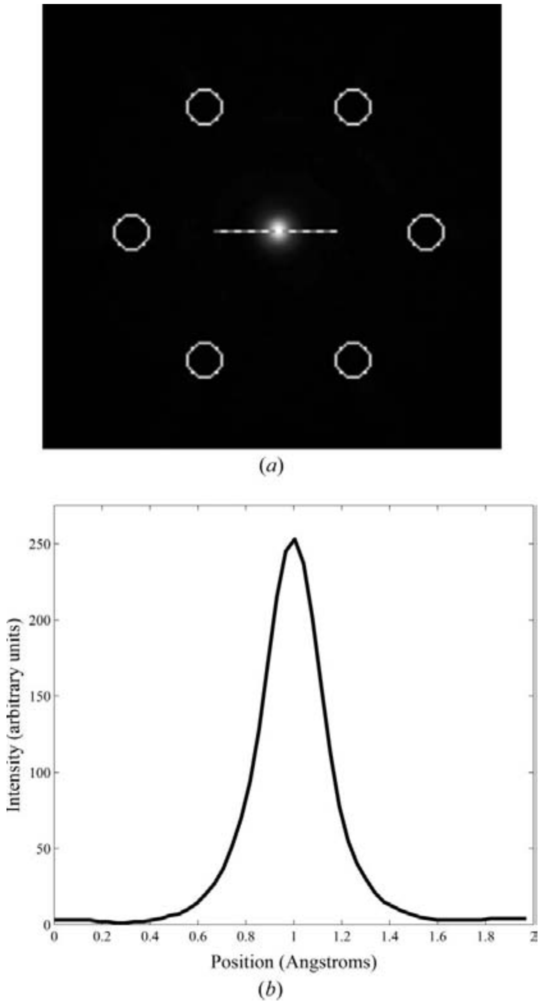

Figure 2
(*a*) Multislice frozen phonon simulated exit wave for a STEM probe incident on an atom column in a 100 Å-thick [111]-oriented Fe specimen. The approximate positions of the six neighbouring atom columns are indicated by the open circles. The electron intensity was extracted across the dashed line in (*a*) and is shown in (*b*).

phonon simulations. Fig. 2(*b*) is a trace of the electron beam intensity extracted along the dashed line in Fig. 2(*a*). The electron beam intensity has a full width at tenth-maximum of only 0.6 Å. This suggests that scattering to the neighbouring atom columns is weak and hence justifies the use of the column approximation for the substitutional atom. The column approximation should be less rigorous for an interstitial atom owing to a lack of STEM probe channelling as well as a shorter distance to the nearest-neighbour atom column (Fig. 1*b*). However, a comparison of the Bloch wave results with multislice simulations nevertheless showed good qualitative agreement (§3.2).

Fig. 3 shows the *Pendellösung* for a STEM probe positioned over an atom column in a perfect [111]-Fe crystal calculated using the Bloch wave and multislice frozen phonon methods. Kirkland's (1998) *autoslic* software was used for the multislice simulations where the output was in the form of a two-dimensional cross section of the beam spreading through the thickness of the foil. The values of five pixels across the $[11\bar{2}]$ in-plane dimension (see Fig. 1*b*) centred about the probe incident position was summed to give the electron intensity at any given depth. The total length of the five pixels is approximately 0.2 Å. For a direct comparison the multislice intensity at the entrance surface of the specimen was normalized to the Bloch wave value in Fig. 3. A STEM probe positioned over an atom column shows alternating intensity maxima and minima as it propagates through the foil thickness. In the Bloch wave calculation the maxima are at 18 and 66 Å while a minimum occurs at 46 Å. In the multislice simulations the maxima are at approximately 17 and 65 Å while the minimum is at approximately 43 Å. Furthermore, the intensities of the maxima and minima are not exact between Bloch wave and multislice simulations but the qualitative agreement is good. This suggests that the TDS is adequately modelled using the Bloch wave phenomenological approach. The substitutional W dopant atom is positioned at depths corresponding to the intensity maxima and minima, *i.e.* 18, 46 and 66 Å.

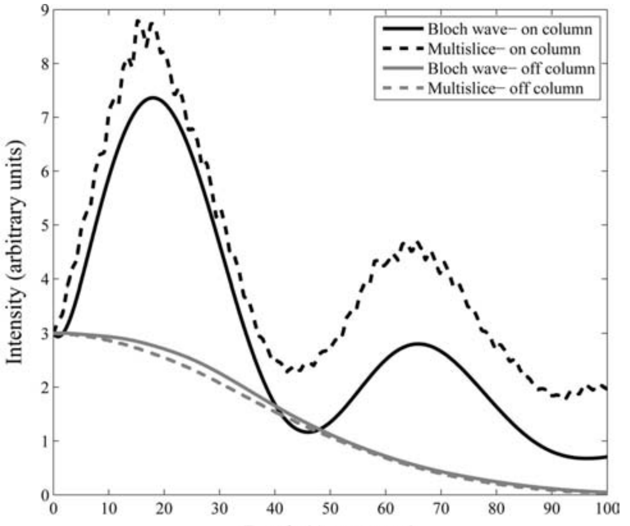

Figure 3
Pendellösung plots for a STEM probe in a perfect [111]-Fe crystal. Plots for a probe incident on an atom column and off an atom column are shown. The position of the off-column probe coincides with that of an interstitial atom (Fig. 1*b*). Results from Bloch wave calculations as well as multislice frozen phonon simulations are presented. The electron intensity at the specimen entrance surface from multislice simulations has been normalized to the Bloch wave value.

Fig. 4(*a*) shows the Bloch wave calculated STEM probe *Pendellösung* for the atom column containing a W substitutional dopant atom at a depth of 18 Å in an otherwise perfect [111]-Fe specimen. Figs. 4(*b*) and 4(*c*) are the equivalent plots for substitutional W atoms at depths of 46 and 66 Å, respectively. In Fig. 4(*d*) the change in the *Pendellösung* intensity, with respect to the perfect crystal, for the 18, 46 and 66 Å depth substitutional W atoms are superimposed. There is a sharp drop in the electron intensity at the dopant atom position followed by a broad peak labelled A at *greater* depth. For the 18 Å depth dopant atom peak A is at 22 Å while for the 46 and 66 Å depth dopant atoms the peaks are at 54 and 71 Å, respectively. At depths beyond peak A the curve shows an oscillatory behaviour that is largely periodic and also largely negative. As an example for the 18 Å depth dopant atom a maximum is present at 52 Å and two minima are present at 36 and 74 Å giving a periodicity of approximately 38 Å. This is a similar magnitude to the 48 Å periodicity observed between the intensity maxima for the STEM probe *Pendellösung* in a perfect crystal (Fig. 3). Furthermore, the magnitude of the intensity dip at the dopant atom position appears to increase monotonically with the STEM probe intensity at that depth (Fig. 3).

A heavier W atom leads to increased high-angle TDS scattering compared with the host Fe atoms and hence there should be a decrease in the local electron intensity at the dopant atom position. This could be the origin of the sharp intensity dip observed at the dopant atom position in Fig. 4(*d*). In the Bloch wave perturbation theory the imaginary part of the excess potential term υ (§2) models the change in TDS scattering owing to the dopant atom. Hence if the Bloch wave simulations are carried out ignoring this imaginary term the intensity dip should largely disappear. Fig. 5 shows the change in electron intensity as a function of depth calculated in a similar manner to Fig. 4(*d*) but with the imaginary part of the excess potential set to zero. As expected the intensity dip at the dopant atom has largely disappeared [a small dip is still seen for the 46 and 66 Å depth dopant atoms but these are not significant compared with the magnitudes observed in Fig. 4(*d*)]. The remaining gross features of the curves in Fig. 5 are, however, consistent with Fig. 4(*d*).

Although the heavier W dopant atom leads to increased TDS scattering its higher atomic number should also Coulomb attract the surrounding STEM probe intensity. A similar effect is observed during channelling of a STEM probe positioned over an atom column. For the STEM probe parameters used in this study the 'atom focusing' effect for a perfect [111]-b.c.c. Fe crystal takes place at a depth of 18 Å (Fig. 3). A similar *Pendellösung* calculation for [111]-b.c.c. W revealed a shorter atom focusing distance of 10 Å owing to stronger focusing by the higher atomic number of W compared with Fe (the atom

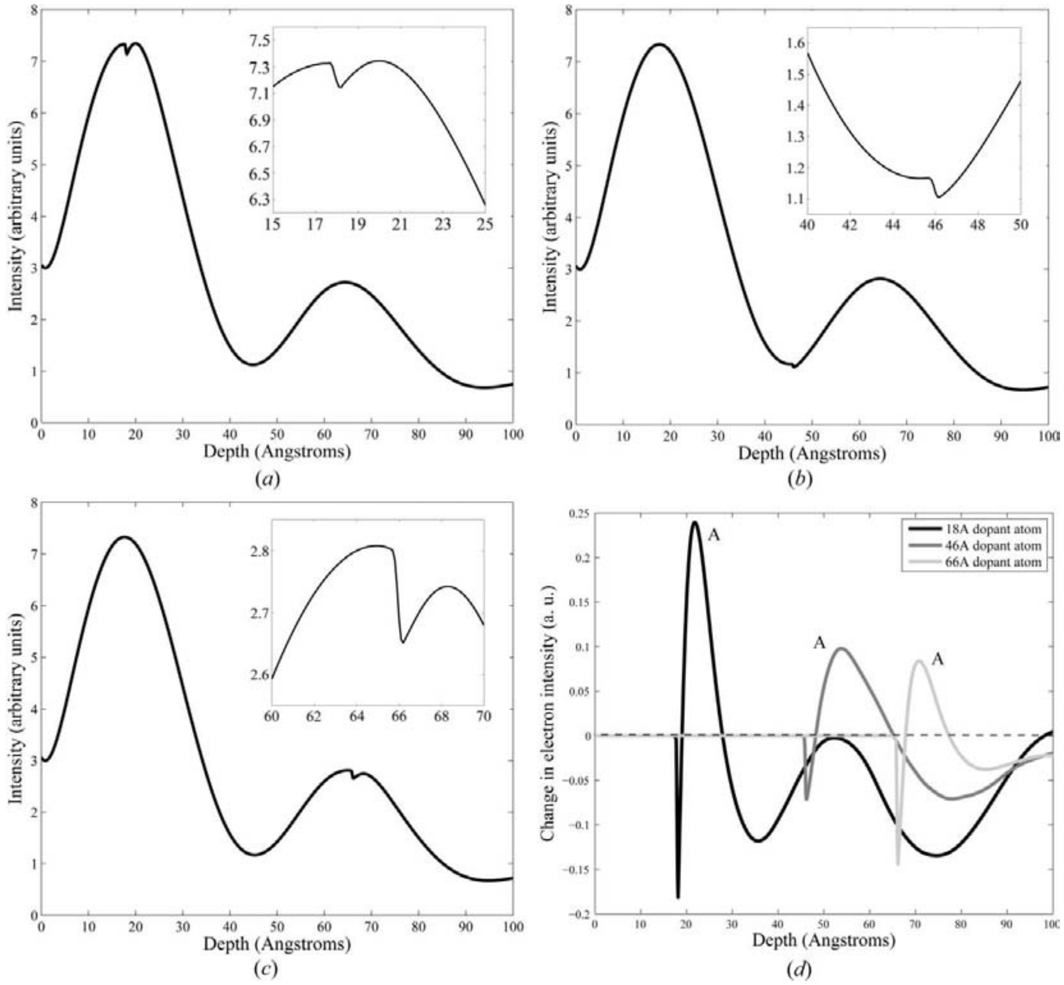

Figure 4
Bloch wave calculated *Pendellösung* plots for a STEM probe positioned on an atom column containing a substitutional W dopant atom in a 100 Å-thick [111]-Fe crystal. In (*a*), (*b*) and (*c*) the results for a W atom at depths of 18, 46 and 66 Å, respectively, are shown. The inset in each figure is a magnified view of the *Pendellösung* close to the depth of the dopant atom. In (*d*) the change in electron intensity for the defect crystals in (*a*)–(*c*) with respect to the perfect crystal are plotted as a function of depth.

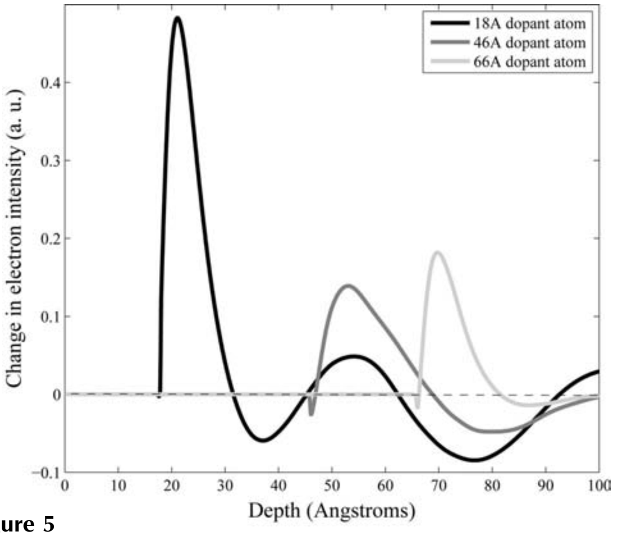

Figure 5
The change in electron intensity with respect to a perfect crystal is plotted as a function of depth for a STEM probe positioned on a [111]-Fe atom column containing a substitutional W atom at depths of 18, 46 and 66 Å, respectively. When calculating the *Pendellösung* for the defect crystal using the Bloch wave model the imaginary part of the excess potential υ was set to zero [equation (2)].

spacing along [111] is similar for both W and Fe, *i.e.* 2.7 and 2.5 Å, respectively). This suggests that peak A in Fig. 4(*d*) represents a similar atom focusing effect owing to the W substitutional atom Coulomb attracting the neighbouring electron intensity.

In equation (4) the STEM probe wavefunction at a given depth is expressed as the sum of individual contributions from each Bloch state. In Figs. 6(*a*) and 6(*b*) the STEM probe *Pendellösung* owing to the 1*s* and non-1*s* states are shown for an atom column containing a substitutional W dopant atom at 18 Å depth. The 1*s* state shows a sharp drop in intensity at the dopant atom while the non-1*s* state shows a broad peak at a depth beyond the dopant atom. In Fig. 6(*c*) the change in 1*s* state electron intensity, with respect to a perfect crystal, is plotted as a function of depth for an atom column containing a substitutional W atom. The curves for dopant atoms at depths of 18, 46 and 66 Å are superimposed in Fig. 6(*c*). The magnitude of the 1*s* state intensity dip at the dopant atom is almost equal for the 46 and 66 Å depth dopant atoms, while in Fig. 4(*d*) it is twice as large for the 66 Å depth dopant atom

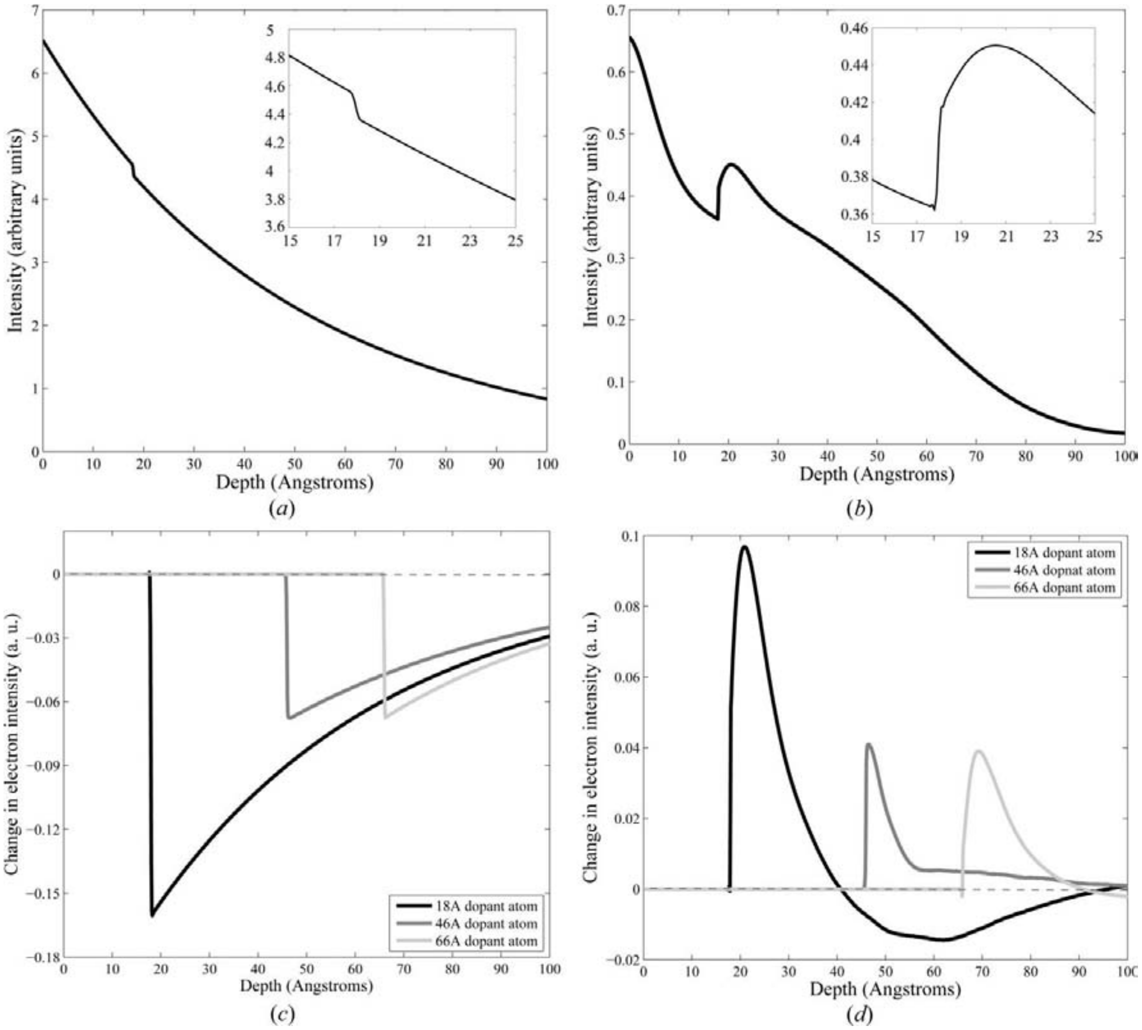

Figure 6
(*a*) and (*b*) are *Pendellösung* plots for the STEM wavefunction due to the 1*s* and non-1*s* states, respectively, for a probe positioned on a [111]-Fe atom column containing a substitutional W atom at 18 Å depth. The inset in each figure is a magnified view of the *Pendellösung* close to the depth of the dopant atom. In (*c*) and (*d*) the change in 1*s* and non-1*s* state intensity for a defect crystal with respect to the perfect crystal is plotted as a function of depth. The defect crystal is [111]-Fe containing a substitutional W atom at a depth of 18, 46 and 66 Å.

compared with the dopant atom at 46 Å. Fig. 6(*d*) shows the change in non-1*s* state electron intensity for a defect crystal compared with a perfect crystal as a function of depth. Curves for substitutional W atoms at depths of 18, 46 and 66 Å are superimposed. The non-1*s* state intensity peaks at 21 and 69 Å for the 18 and 66 Å depth dopant atoms, respectively, and is in good agreement with the values obtained for peak A in Fig. 4(*d*) (*i.e.* 22 and 71 Å, respectively). The change in the non-1*s* state intensity for the 46 Å depth dopant atom is, however, more 'saw-tooth' like in shape and hence peaks virtually at the dopant atom position. The sharp increase in the non-1*s* state intensity would partly offset the decrease in 1*s* state intensity so that overall the net change in electron intensity at the dopant atom position is least for the 46 Å depth dopant atom (Fig. 4*d*). Note also that Figs. 6(*c*) and 6(*d*) do not show the same intensity oscillations which are evident in Fig. 4(*d*) following peak A. Hence these intensity oscillations must be due to periodic 'beating' of the 1*s* and non-1*s* Bloch waves at various depths within the specimen. The results of Figs. 6(*c*) and 6(*d*) indicate that the W substitutional atom preferentially TDS scatters the 1*s* Bloch state, which is tightly bound to the atom column, to high angles and Coulomb attracts the non-1*s* states, which largely channel through the spaces between the atom columns, towards it.

Equation (1) indicates that high-angle scattering should increase monotonically with the local electron beam intensity at the depth of the dopant atom and the results in Figs. 4(*d*) and 6(*c*) appear to confirm this. At depths corresponding to the *Pendellösung* maxima (*i.e.* 18 and 66 Å) it is found that the STEM wavefunction due to the 1*s* Bloch state is in phase with the wavefunction due to all non-1*s* states so that constructive interference takes place. For *Pendellösung* minima (*i.e.* 46 Å), however, the wavefunction due to the 1*s* state and all non-1*s* states are out of phase and destructive interference takes place. High-angle scattering for a substitutional atom takes place predominantly through a perturbation in the 1*s* state STEM wavefunction ($\Delta\Psi^{1s}$) at the dopant atom depth $z_{\rm dop}$ which, following equations (2) and (4), can be expressed as

$$\Delta\Psi^{1s}(\mathbf{R}, z_{\rm dop}) = \int \Delta\varepsilon^{1s}\big(\mathbf{k}_{\rm t}, z_{\rm dop}\big) b^{1s}(\mathbf{k}_{\rm t}, \mathbf{R}) \times \exp\big[2\pi i\big(k_z + \gamma^{1s}\big) z_{\rm dop}\big] \times \exp(-2\pi i \mathbf{k}_{\rm t}\cdot\mathbf{R}_{\rm o})\, {\rm d}\mathbf{k}_{\rm t}\,, \qquad (5)$$

and

$$\Delta\varepsilon^{1s}\big(\mathbf{k}_{\rm t}, z_{\rm dop}\big) = (2\pi i m e/h^2 k_z)\Delta z \times \sum_p \varepsilon^p(\mathbf{k}_{\rm t}, z_{\rm dop})\exp\big[2\pi i\big(\gamma^p - \gamma^{1s}\big) z_{\rm dop}\big] \times \int b^p(\mathbf{k}_{\rm t}, \mathbf{R})\upsilon(\mathbf{R}, z_{\rm dop}) b^{1s}(\mathbf{k}_{\rm t}, \mathbf{R})^*\, {\rm d}\mathbf{R},$$

where Δz is the slice thickness used in the calculations (*i.e.* 0.1 Å; §2). Assume that the excess potential υ of the dopant atom is a delta function so that

$$\Delta\varepsilon^{1s}\big(\mathbf{k}_{\rm t}, z_{\rm dop}\big) \simeq \frac{2\pi i m e}{h^2 k_z}\upsilon\Delta z \sum_p \varepsilon^p(\mathbf{k}_{\rm t}, z_{\rm dop}) \times \exp\big[2\pi i\big(\gamma^p - \gamma^{1s}\big) z_{\rm dop}\big] \times b^p(\mathbf{k}_{\rm t}, \mathbf{R}_{\rm dop}) b^{1s}(\mathbf{k}_{\rm t}, \mathbf{R}_{\rm dop})^*, \qquad (6)$$

where $\mathbf{R}_{\rm dop}$ is the two-dimensional position vector of the dopant atom. For a STEM probe incident at the dopant atom position, $\mathbf{R}_{\rm o} = \mathbf{R}_{\rm dop}$. The STEM probe wavefunction, $\Delta\Psi^{1s}(\mathbf{R}_{\rm dop})$, for this case can be determined approximately by substitution of (6). Hence,

$$\Delta\Psi^{1s}(\mathbf{R}_{\rm dop}, z_{\rm dop}) \simeq \frac{2\pi i m e \upsilon\Delta z}{h^2 k_z}\big|b^{1s}(\mathbf{R}_{\rm dop})\big|^2 \times \bigg\{\sum_p \int \varepsilon^p(\mathbf{k}_{\rm t}, z_{\rm dop}) b^p(\mathbf{k}_{\rm t}, \mathbf{R}_{\rm dop}) \times \exp\big[2\pi i\big(k_z + \gamma^p\big) z_{\rm dop}\big] \times \exp\big(-2\pi i \mathbf{k}_{\rm t}\cdot\mathbf{R}_{\rm dop}\big)\, {\rm d}\mathbf{k}_{\rm t}\bigg\}, \qquad (7)$$

where $|b^{1s}(\mathbf{R}_{\rm dop})|^2$ is the square modulus of the 1s Bloch state at the position $\mathbf{R}_{\rm dop}$. The 1s Bloch state is non-dispersive (Pennycook & Jesson, 1991) and hence its square modulus is largely independent of $\mathbf{k}_{\rm t}$ so that the term can be placed outside the integral in (7). Furthermore it is reasonably assumed that $(1/k_z)$ is approximately constant within the 20 mrad STEM objective aperture. The expression within the curly brackets of (7) has the same form as (4). Hence $\Delta\Psi^{1s}(\mathbf{R}_{\rm dop})$ shows a similar dependence with respect to $z_{\rm dop}$ as the STEM probe *Pendellösung* for a perfect crystal. Equations (1) and (7) predict that the high-angle scattering is directly proportional to the local electron beam intensity. In Fig. 3 the Bloch wave calculated STEM probe intensity varies as 6.3:1.0:2.4 at depths of 18, 46 and 66 Å, respectively. However, the magnitude of the 1s state intensity dip, and hence 'high-angle' scattering, in Fig. 6(*c*), varies as 2.4:1.0:1.0 for the 18, 46 and 66 Å depth dopant atoms, indicating that the linear relationship with the electron beam intensity is not strictly valid. This highlights the limitations of the various approximations used in deriving (7). In particular, the 1s Bloch state and excess potential will vary rapidly on a similar spatial scale and hence, strictly speaking, υ cannot be treated as a delta function. Nevertheless the above analysis provides important insight into the variation of high-angle scattering with respect to local electron beam intensity, *i.e.* at a *Pendellösung* maximum the 1s and non-1s Bloch states are in phase so that the local electron beam intensity and high-angle scattering are maximized and conversely for a *Pendellösung* minimum.

Before concluding this section, results from multislice frozen phonon simulations are compared with the Bloch wave calculations. Fig. 7(*a*) shows the HAADF intensity trace across the [11$\bar{2}$] direction for a 100 Å-thick [111]-Fe crystal containing a W substitutional dopant atom. HAADF traces are superimposed for supercells containing the W atom at depths of 18, 45 and 65 Å (the dopant atom positions deviate slightly from the Bloch wave values owing to atoms in the multislice supercell having well defined coordinates). The central atom column in Fig. 7(*a*) contains the W dopant atom and has a higher intensity than the neighbouring atom columns (the average intensity of the leftmost and rightmost atom columns was normalized to unity to make a direct comparison between the different HAADF traces). However, the increase in HAADF intensity at the central atom column compared with its neighbours is only 1–2% of the total beam intensity indicating only small amounts of high-angle scattering by the substitutional W atom. The increase in HAADF intensity is approximately 1.7:1.0:1.0 for the 18, 45 and 65 Å depth dopant atoms, which is a similar ratio to that obtained from Fig. 6(*c*). Fig. 7(*b*) shows the multislice simulated STEM probe *Pendellösung* for a supercell containing a substitutional W dopant atom at 18 Å depth (the intensity of five pixels, with a total length of 0.2 Å, was summed at each depth similar to Fig. 3). In Fig. 7(*c*) the change in the (multislice simulated) electron intensity in the defect crystal with respect to the perfect crystal is plotted as a function of depth. Results for dopant atoms at depths of 18, 45 and 65 Å are superimposed. The change in intensity should have a value of zero at all depths shallower than the dopant atom position but inspection of Fig. 7(*c*) shows that this is not the case, particularly for the 45 and 65 Å depth dopant atoms. This indicates that the number of frozen phonon configurations simulated (40 in this case) has only partially converged. Nevertheless a broad peak labelled A representing an increase in electron intensity is clearly evident close to the dopant atom position. For the 18, 45 and 65 Å depth dopant atoms the peak is at approximately 19, 50 and 66 Å, respectively. This peak could therefore represent the atom focusing effect described earlier, although it is an order of magnitude larger compared with peak A in Fig. 4(*d*) [the intensity scales in Figs. 4(*d*) and 7(*c*) can be directly compared]. The oscillations in the intensity difference following peak A in Fig. 7(*c*) are also qualitatively similar to that observed in Fig. 4(*d*). However, it is interesting to note that the sharp intensity dip observed at the dopant atom position in Fig. 4(*d*) is not visible in Fig. 7(*c*). This is most likely due to 'noise' in the frozen phonon *Pendellösung* plots. Recall that the excess high-angle scattering by the substitutional W atom is only 1–2% of the total beam intensity and, furthermore, when generating the multislice *Pendellösung* plots using the *autoslic* code only a two-dimensional cross section of the beam spreading, rather than the complete three-dimensional

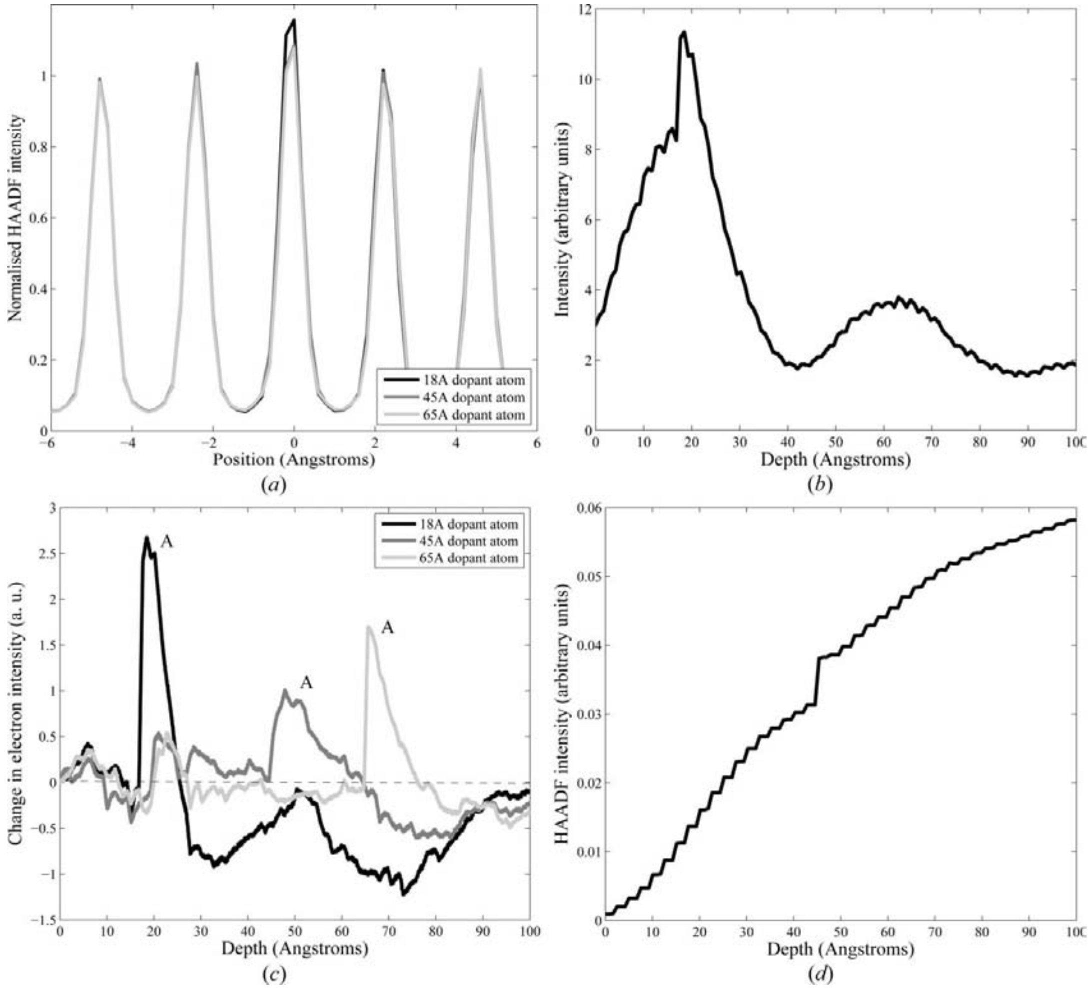

Figure 7
(*a*) shows traces of the multislice frozen phonon simulated HAADF intensity along the [11$\bar{2}$] direction of a 100 Å-thick [111]-oriented Fe crystal containing a substitutional W atom at depths of 18, 45 and 65 Å. The atom column containing the W atom is at the arbitrary position of 0 Å and the average intensity of the leftmost and rightmost atom columns has been normalized to a value of unity. (*b*) shows the multislice simulated *Pendellösung* for a STEM probe incident on an atom column in [111]-Fe that contains a substitutional W atom at 18 Å depth. In (*c*) the change in multislice simulated electron intensity for a defect crystal with respect to the perfect crystal is plotted as a function of depth for substitutional W atoms at 18, 45 and 65 Å depth. (*d*) plots the 'measured' HAADF intensity as a function of depth for a probe positioned on the atom column containing the 45 Å depth substitutional W atom. A step change increase in the HAADF intensity is observed at the depth of the dopant atom.

data, is available. In Fig. 7(*d*) the multislice simulated HAADF signal from a STEM probe positioned over an atom column containing a substitutional W dopant atom at 45 Å depth is plotted as a function of depth. The HAADF signal shows a step change increase at precisely the dopant atom position. This provides evidence that high-angle scattering is indeed taking place at the dopant atom position prior to peak A in Fig. 7(*c*), which for the 45 Å depth dopant atom occurs at approximately 50 Å.

3.2. STEM probe *Pendellösung* for interstitial W in [111]-Fe

In this section, scattering by an interstitial W atom in [111]-oriented Fe is investigated. Fig. 3 shows the Bloch wave and multislice simulated *Pendellösung* for a STEM probe in a perfect [111]-Fe specimen with the probe position coinciding with that of an interstitial atom (Fig. 1*b*). The STEM probe intensity decreases monotonically with depth. Simulations are carried out for an interstitial W atom at depths of 18 and 46 Å. Fig. 8(*a*) shows the Bloch wave calculated *Pendellösung* for an 18 Å depth interstitial W atom in [111]-Fe. In Fig. 8(*b*) the change in electron intensity for the defect crystal with respect to the perfect crystal is plotted as a function of depth. Curves for dopant atoms at 18 and 46 Å depths are superimposed. A sharp decrease in the electron intensity is observed at the dopant atom position followed by a broad peak labelled A. Peak A is at 22 and 51 Å for the 18 and 46 Å depth dopant atoms, respectively. The magnitude of the intensity decrease is larger for the 18 Å depth dopant atom which also has the higher local electron beam intensity in a perfect crystal compared with the 46 Å depth dopant atom (Fig. 3). The decrease in intensity is due to localized high-angle TDS scattering by the heavy W atom while peak A represents an atom focusing effect. Changes to the 1*s* and non-1*s* Bloch state intensities were also analysed along the lines described previously in §3.1. The 1*s* Bloch state modulus at the specimen entrance surface was smaller by two orders of magnitude compared with the net modulus of all non-1*s* states and

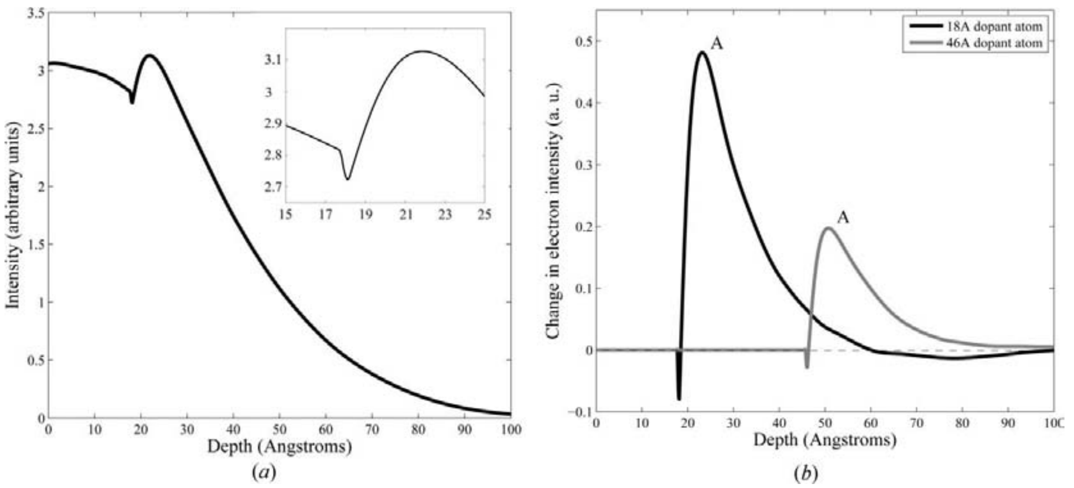

Figure 8

(*a*) shows the Bloch wave calculated *Pendellösung* for a STEM probe positioned over a 18 Å depth interstitial W atom in [111]-Fe. The inset is a magnified view of the *Pendellösung* close to the depth of the dopant atom. In (*b*) the change in electron intensity for a defect crystal with respect to the perfect crystal is plotted as a function of depth. The defect crystal contains an interstitial W atom at 18 and 46 Å depths.

furthermore showed hardly any change due to dopant atom scattering. This indicates that the electrostatic potential of an interstitial W atom is not sufficiently strong to attract the 1*s* state electron intensity, which is tightly bound to the neighbouring atom columns, towards it. The non-1*s* states are therefore collectively responsible for the high-angle TDS scattering and atom focusing effect of the interstitial dopant atom.

Fig. 9(*a*) shows HAADF intensity traces along the $[11\bar{2}]$ direction of a [111]-Fe specimen containing an interstitial W atom at 18 and 46 Å depths. Multislice frozen phonon simulations were used to generate the HAADF traces. In Fig. 9(*a*) the dopant atom is at the (arbitrary) position of 1 Å. The 18 Å depth dopant atom shows greater contrast above background compared with the 46 Å depth dopant atom, but the increase in the high-angle scattered intensity is less than 1% of the total electron beam intensity. The increase in HAADF intensity is in the ratio 1.9:1.0 for the 18 and 46 Å depth dopant atoms, while the corresponding ratio for the intensity dip in Fig. 8(*b*) has a slightly larger value of 2.8:1.0. This suggests that high-angle scattering by an interstitial atom varies monotonically with the local electron beam intensity (Fig. 3). Fig. 9(*b*) shows the multislice simulated *Pendellösung* for a STEM probe incident directly at the interstitial atom position (at each depth the values of five pixels covering a dimension of 0.2 Å were summed similar to Fig. 3). The W interstitial is at a depth of 18 Å. An increase in the electron intensity is observed at depths slightly greater than that of the dopant atom. In Fig. 9(*c*) the change in the multislice simulated electron intensity owing to scattering by 18 and 46 Å depth interstitial W atoms is plotted as a function of depth. The change in intensity at depths shallower than the dopant atom is almost zero, indicating that the frozen phonon simulations have sufficiently converged. A broad peak labelled A is observed at 21 and 50 Å for the 18 and 46 Å depth dopant atoms, respectively. The position of peak A as well as the overall shape of the curves in Fig. 9(*c*) are consistent with the Bloch wave calculations (Fig. 8*b*). However, the intensity of peak A in Fig. 9(*c*) is several times larger than that in Fig. 8(*b*) and the sharp intensity dip at the dopant atom position owing to 'high-angle' scattering is not observed in the multislice results. This could be due to the small amount of excess high-angle scattering produced by the dopant atom (<1% of the total electron beam intensity) as well as the manner in which *Pendellösung* plots are generated using the *autoslic* program (Kirkland, 1998). However, a plot of the HAADF intensity as a function of depth showed a step change increase at the dopant atom position, similar to Fig. 7(*d*), which indicates that localized excess high-angle scattering by the interstitial atom does in fact take place.

3.3. Bloch wave scattering mechanisms for substitutional and interstitial dopant atoms

In this section Bloch wave scattering mechanisms, such as intraband and interband scattering, are investigated (Hirsch *et al.*, 1965). Results are presented for a substitutional and interstitial W atom at a depth of 18 Å in [111]-Fe. From equation (4) the STEM probe wavefunction (Ψ^q) owing to a single Bloch state q in the perfect crystal is

$$\Psi^q(\mathbf{R}, z) = \int \varepsilon^q(\mathbf{k}_t) b^q(\mathbf{k}_t, \mathbf{R}) \exp\left[2\pi i\left(k_z + \gamma^q\right)z\right] \times \exp(-2\pi i \mathbf{k}_t \cdot \mathbf{R}_o)\, \mathrm{d}\mathbf{k}_t, \qquad (8)$$

where the excitation ε is now independent of z since (8) is evaluated for a perfect crystal. The modulus of Ψ^q is an approximate measure of the contribution of the Bloch state q towards the STEM probe intensity. The integral is evaluated for $z = 18$ Å. Fig. 10(*a*) plots the modulus of Ψ^q as a function of Bloch state index for a probe positioned over an atom column in [111]-Fe. The Bloch state indices are assigned according to their position in the dispersion surface. Bloch

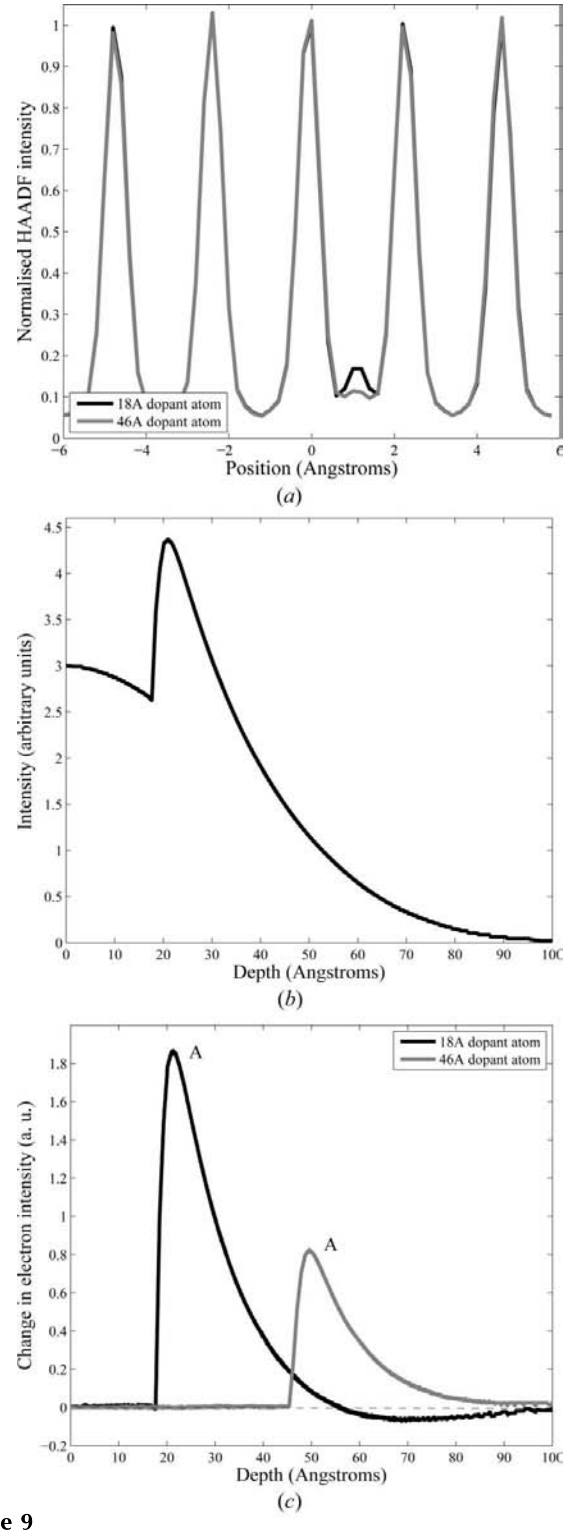

Figure 9
(*a*) shows traces of the multislice frozen phonon simulated HAADF intensity along the $[11\bar{2}]$ direction of a 100 Å-thick [111]-oriented Fe crystal containing an interstitial W atom at depths of 18 and 46 Å. The interstitial atom is at the arbitrary position of 1 Å and the average intensity of the leftmost and rightmost atom columns has been normalized to a value of unity. In (*b*) the multislice simulated *Pendellösung* plot for a STEM probe positioned on an interstitial W atom at 18 Å depth is shown. The change in electron intensity for the defect crystal with respect to the perfect crystal is shown as a function of depth in (*c*). The defect crystal contains an interstitial W atom at 18 and 46 Å depths.

state 1, with the largest value of γ, is the 1*s* state. In Fig. 10(*a*) the modulus of the 1*s* state is substantially larger than the other non-1*s* states. Fig. 10(*b*) plots the modulus of Ψ^q as a function of Bloch state index for a probe positioned between the atom columns in [111]-Fe. The position of the probe coincides with that of an interstitial atom in a defect crystal (Fig. 1*b*). The modulus of the 1*s* state is small in comparison with Fig. 10(*a*) but the non-1*s* Bloch states with indices 4 to approximately 16 are excited by the probe. The maximum modulus of the non-1*s* states in Fig. 10(*b*) is, however, an order of magnitude smaller compared with the 1*s* state modulus in Fig. 10(*a*).

Now consider the change in the STEM probe wavefunction owing to dopant atom scattering. Each Bloch state q will perturb the probe wavefunction by $\Delta\Psi^q$ which following (4) can be expressed as

$$\Delta\Psi^q(\mathbf{R},z) = \int \Delta\varepsilon^q(\mathbf{k}_t,z) b^q(\mathbf{k}_t,\mathbf{R}) \exp\big[2\pi i\big(k_z+\gamma^q\big)z\big] \times \exp(-2\pi i\mathbf{k}_t\cdot\mathbf{R}_o)\,\mathrm{d}\mathbf{k}_t, \tag{9}$$

where the change in excitation $\Delta\varepsilon^q$ is calculated by multiplying the right-hand side of (2) by the slice thickness Δz (= 0.1 Å). Equation (9) is evaluated at the dopant atom depth of 18 Å. In Fig. 10(*c*) the modulus of $\Delta\Psi^q$ is plotted as a function of Bloch state index for a probe positioned on an atom column in [111]-Fe containing a substitutional W atom. The 1*s* state modulus is at least an order of magnitude larger than the non-1*s* states. Fig. 10(*d*) plots the modulus of $\Delta\Psi^q$ as a function of Bloch state index for a probe incident at the W interstitial atom position (z = 18 Å) in [111]-Fe. The 1*s* state modulus is zero but many more non-1*s* states are found to contribute to dopant atom scattering compared with scattering by a perfect crystal (Fig. 10*b*).

Equation (2) indicates that each Bloch state p will contribute to the change in the excitation of the qth Bloch state $\Delta\varepsilon^q$ during dopant atom scattering. The $p = q$ term represents intraband scattering while $p \neq q$ terms denote interband scattering. For strong scattering at a given incident electron wavevector two criteria must be satisfied. The scattered Bloch wave p must have a non-zero excitation and the integral in (2) must also be large, *i.e.* both Bloch waves p and q must have significant electron intensity at the dopant atom position. Bloch wave scattering can be further analysed using the following parameters evaluated at the depth z of the dopant atom,

$$\begin{aligned} I^{p,q}(\mathbf{k}_t) &= \int b^p(\mathbf{k}_t,\mathbf{R})\upsilon(\mathbf{R})b^q(\mathbf{k}_t,\mathbf{R})^*\,\mathrm{d}\mathbf{R}, \\ S^{p,q}(\mathbf{k}_t) &= \frac{\varepsilon^p(\mathbf{k}_t)}{k_z}\,I^{p,q}(\mathbf{k}_t). \end{aligned} \tag{10}$$

First consider the case of a substitutional W atom. Fig. 10(*c*) indicates that the 1*s* state undergoes the largest change in modulus and Fig. 6(*c*) indicates that it is the 1*s* state that is responsible for the excess high-angle TDS scattering. Hence, intra- and interband scattering to the 1*s* Bloch state will be analysed in more detail. Fig. 11(*a*) shows the 1*s* Bloch state electron intensity distribution in a [111]-oriented Fe crystal for

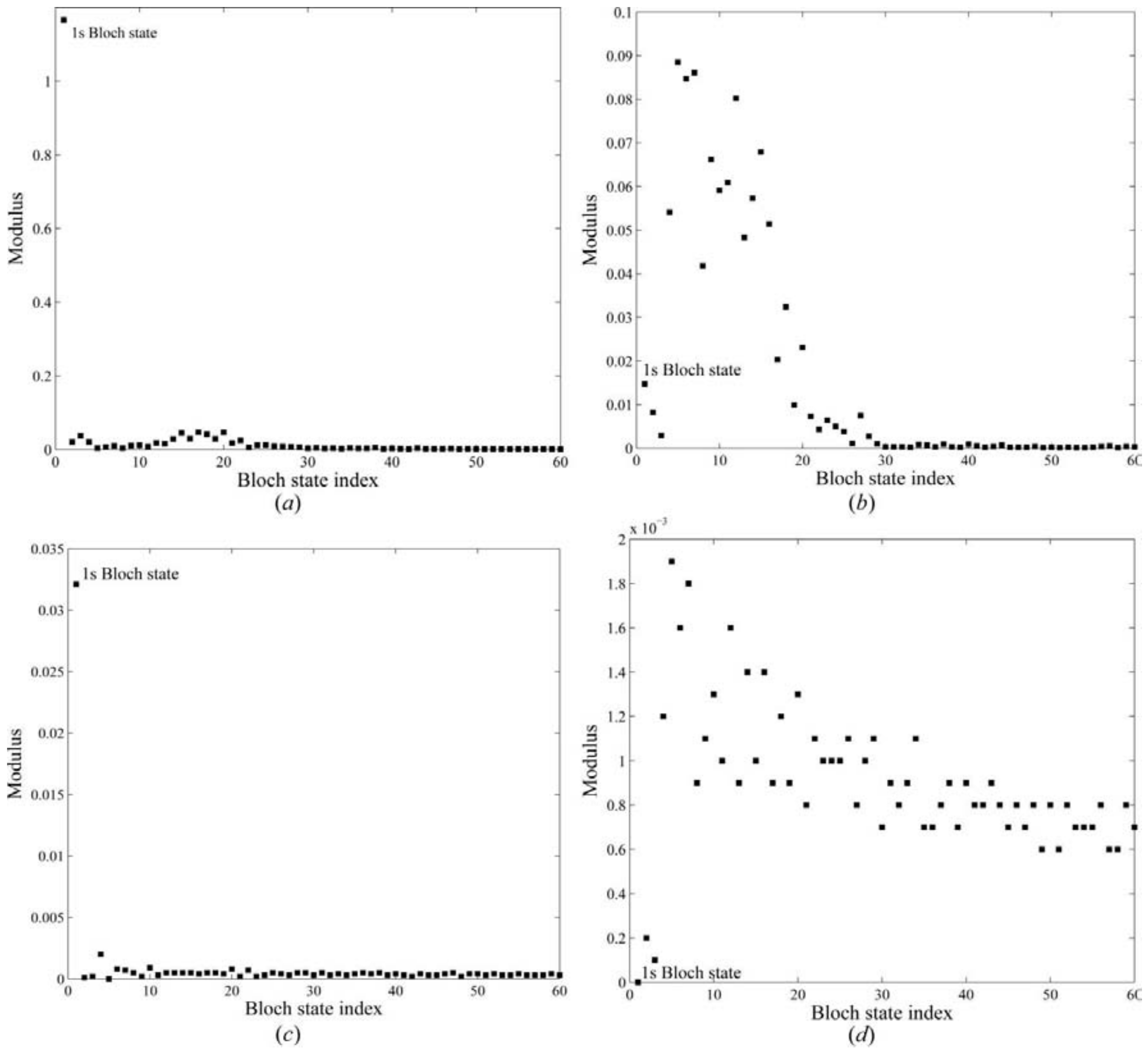

(a) (b)
(c) (d)

Figure 10
(*a*) and (*b*) show the modulus of Ψ^q at 18 Å depth as a function of Bloch state index for a STEM probe incident on an atom column and at the position of an interstitial atom (Fig. 1*b*) in a [111]-oriented perfect Fe crystal, respectively. In (*c*) and (*d*) the modulus of $\Delta\Psi^q$ is plotted as a function of Bloch state index for a substitutional and interstitial W atom in [111]-Fe, respectively. The W atom is at a depth of 18 Å. To aid visualization only the moduli of the first 60 Bloch states are displayed in each figure. See text for more details.

an incident electron wavevector parallel to the optic axis. The electron intensity is highest at the atom column positions. Figs. 11(*b*) and 11(*c*) show $I^{1,1}$ and $S^{1,1}$ for intraband scattering of the 1*s* state by a substitutional W atom. The horizontal and vertical axes represent the component of $\mathbf{k}_t$ along the $[11\bar{2}]^*$ and $[\bar{1}10]^*$ reciprocal-lattice vectors, respectively. $I^{1,1}$ has its maximum value at normal electron beam incidence and slowly decays for larger $\mathbf{k}_t$. The excitation of the 1*s* Bloch state, $\varepsilon^1(\mathbf{k}_t)$, shows a similar variation with respect to $\mathbf{k}_t$ and hence $S^{1,1}$ as well (Fig. 11*c*). It is clear that the strongest intraband scattering takes place at small $\mathbf{k}_t$ (*i.e.* ~0.5 Å^{-1} or 10 mrad) while the edges of a large (*e.g.* >30 mrad) STEM objective aperture contribute relatively little in comparison.

Fig. 12(*a*) shows the electron intensity distribution of Bloch state 4 for an incident electron wavevector parallel to the optic axis. For normal beam incidence this is the most strongly excited Bloch state in [111]-Fe (Mendis, 2008; Mendis & Hemker, 2008) and could therefore potentially undergo strong interband scattering to the 1*s* Bloch state. Fig. 12(*a*) indicates that a significant fraction of the electron intensity for Bloch state 4 is located between the atom columns, but there is some intensity on the atom columns as well. However, unlike the 1*s* state, which is tightly bound to the atom columns, the intensity distribution of Bloch state 4 changes somewhat with $\mathbf{k}_t$ (Pennycook & Jesson, 1991). The variation has a periodicity of **g** along a given reciprocal-lattice direction (Hirsch *et al.*, 1965). Figs. 12(*c*) and 12(*d*) are the $I^{4,1}$ and $S^{4,1}$ plots for interband scattering of Bloch state 4 to the 1*s* state by a substitutional W atom. The maximum value of $I^{1,1}$ is larger than that of $I^{4,1}$ by a factor of 3.8. $S^{4,1}$ is greatest for small $\mathbf{k}_t$ (*i.e.* ~0.25 Å^{-1} or 5 mrad) but in general decreases rapidly for more tilted illumination. This is largely due to the excitation of Bloch state 4 which shows a similar behaviour. However, the maximum value of $S^{4,1}$ is less than that of $S^{1,1}$ by a factor of two despite Bloch state 4 having the highest excitation of all Bloch waves at normal electron beam incidence. Interband scattering from

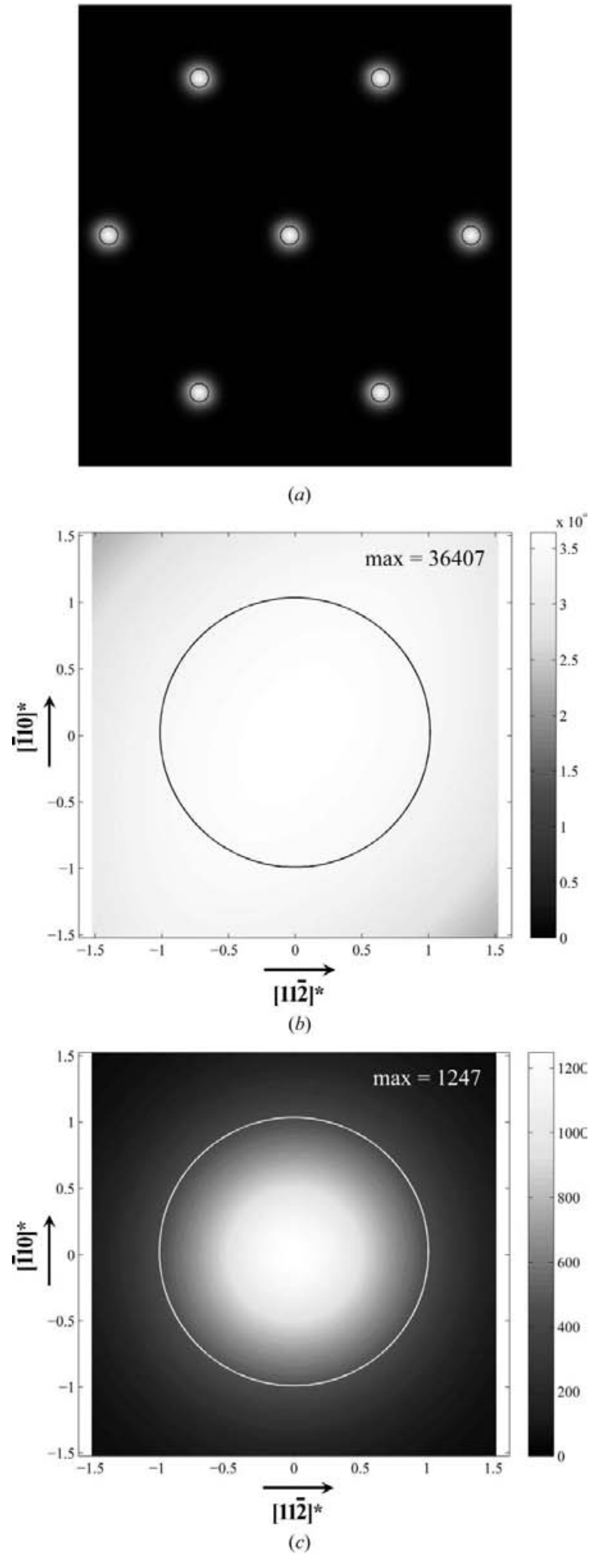

Figure 11
(*a*) shows the electron intensity distribution of the 1*s* Bloch state at normal electron beam incidence in [111]-Fe. The atom column positions are indicated by the open circles. (*b*) and (*c*) show $I^{1,1}$ and $S^{1,1}$, respectively, for a substitutional W atom. The horizontal and vertical axes represent the component of $\mathbf{k}_t$ along the $[11\bar{2}]^*$ and $[\bar{1}10]^*$ reciprocal-lattice vectors, respectively ($\mathbf{k}_t$ is in Å^{-1} and the half width of the image corresponds to 30 mrad at 300 kV). The boundary of a 20 mrad STEM objective aperture is indicated by the open circle. In each figure the maximum value is indicated in the top right-hand corner.

Bloch state 17, which is an example of a more dispersive non-1*s* state, is also analysed for a substitutional W atom. Fig. 12(*b*) shows the electron intensity distribution for Bloch wave 17 at normal beam incidence and Figs. 12(*e*) and 12(*f*) show the plots for $I^{17,1}$ and $S^{17,1}$. $S^{17,1}$ is only significant at larger $\mathbf{k}_t$ within a thin annular region. Non-1*s* states lying deep within the dispersion surface are excited closer to the STEM objective aperture edge (Peng *et al.*, 2004; Cosgriff & Nellist, 2007) and hence give rise to the behaviour observed in Fig. 12(*f*). The maximum value of $S^{4,1}$ is larger than that of $S^{17,1}$ by a factor of 1.7 which suggests that interband scattering by the non-1*s* states generally decreases with increasing Bloch state index.

For a substitutional atom the magnitude of intraband scattering is greater than that of an individual interband scattering event due largely to the variation in $I^{p,q}$. $I^{p,q}$ will be large if both Bloch states p and q have high intensities at the dopant atom position [equation (10)]. For a substitutional dopant atom, $I^{p,q}$ is therefore maximized for $p = q = 1$. However, although the magnitude of an individual interband scattering event is smaller, many non-1*s* Bloch states could contribute to the process thereby making it as important as intraband scattering {the net interband scattering also depends on the phase term $\exp[2\pi i(\gamma^p - \gamma^1)z]$ in equation (2)}. For example in Fig. 6(*c*) the change in the 1*s* state electron intensity varies non-monotonically with depth, which suggests that intraband scattering is not the only dominant scattering mechanism.

Scattering for an interstitial dopant atom in [111]-Fe is more complex since Fig. 10(*d*) indicates that a large number of non-1*s* states undergo a change in modulus. The 1*s* state, however, has very little intensity between the atom columns and hence appreciable scattering of this Bloch state does not take place. The non-1*s* states are therefore responsible for any high-angle TDS scattering by the interstitial atom (§3.2). Recall that the TDS scattering is due to the imaginary part of the excess potential υ which can be assumed to have a similar spatial variation as the real part of υ, *i.e.* the atomic potential. Hence if $I^{p,q}$ and $S^{p,q}$ are large the $p \rightarrow q$ Bloch wave transition should give rise to high-angle TDS scattering. Consider scattering of Bloch state 4, which is the most strongly excited Bloch wave at normal beam incidence, as a representative example of scattering by the interstitial W atom. Figs. 13(*a*) and 13(*b*) plot $I^{4,4}$ and $S^{4,4}$, respectively, for the intraband transition while Figs. 13(*c*) and 13(*d*) plot $I^{17,4}$ and $S^{17,4}$ as a representative interband transition. Intraband scattering is greatest for $\mathbf{k}_t$ almost parallel to the optic axis (Fig. 13*b*) while interband scattering from Bloch wave 17 is found to occur at larger $\mathbf{k}_t$ (Fig. 13*d*). The maximum value of $S^{4,4}$ is, however, larger than that of $S^{17,4}$ by a factor of 2.6 which suggests that scattering in general becomes weaker as the index of the scattered Bloch wave increases. The maximum value of $S^{1,1}$ for a substitutional atom is greater than that of $S^{4,4}$ for an interstitial atom by a factor of 2.6. However, for an interstitial atom many more Bloch states are scattered (Fig. 10*d*) thereby producing sufficient dopant atom contrast in the HAADF image (Fig. 9*a*).

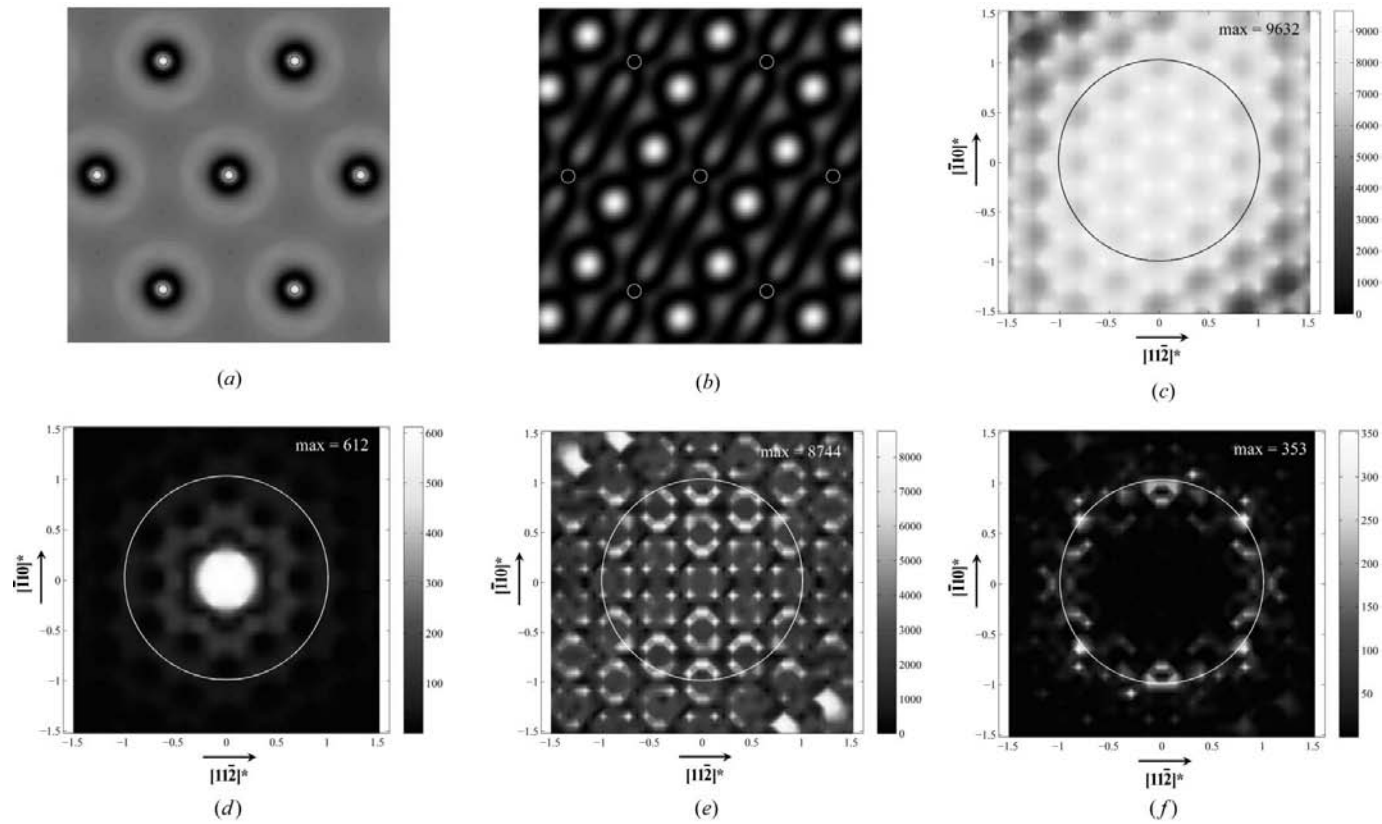

Figure 12
(*a*) and (*b*) show the electron intensity distribution of Bloch waves 4 and 17, respectively, at normal electron beam incidence in [111]-Fe. The atom column positions are indicated by the open circles. (*c*)–(*f*) plot $I^{4,1}$, $S^{4,1}$, $I^{17,1}$ and $S^{17,1}$ for a substitutional W atom. The horizontal and vertical axes represent the component of $\mathbf{k}_t$ along the [11$\bar{2}$]* and [$\bar{1}$10]* reciprocal-lattice vectors, respectively ($\mathbf{k}_t$ is in Å^{-1} and the half width of the image corresponds to 30 mrad at 300 kV). The boundary of a 20 mrad STEM objective aperture is indicated by the open circle. In each figure the maximum value is indicated in the top right-hand corner.

4. Summary and conclusions

A Bloch wave model based on time-dependent perturbation theory was used to analyse scattering by a substitutional and interstitial W atom in [111]-Fe. The results were compared with multislice frozen phonon simulations and generally showed good agreement. For the substitutional atom, high-angle TDS scattering of the 1*s* Bloch state, which is tightly bound to the atom columns, leads to dopant atom contrast in the HAADF image. For the 1*s* state intraband scattering is found to be larger than individual interband scattering events. However, the collective interband scattering of all non-1*s* states is non-negligible and gives rise to variations in the high-angle scattering with depth. In particular, high-angle scattering increases monotonically with the electron beam intensity at the dopant atom position, although Bloch wave and multislice simulations did not provide evidence for the linear relationship predicted by equation (1). The heavy W atom also Coulomb attracts the surrounding electron intensity of the STEM probe, which is largely due to the non-1*s* states, towards it. This leads to an increase in electron intensity following propagation of the probe past the dopant atom. The effect is similar to channelling of a STEM probe along the atom columns of a crystal. For an interstitial W atom in [111]-Fe that lies between the atom columns, the 1*s* state has a negligible effect on scattering. The non-1*s* states are therefore collectively responsible for high-angle TDS scattering as well as Coulomb attraction of the surrounding STEM probe intensity. The magnitude of individual Bloch wave transitions for an interstitial atom are small in comparison with the 1*s* intraband transition for a substitutional atom. However, many non-1*s* Bloch states undergo scattering so that a reasonable dopant atom contrast is evident in the HAADF image provided the electron beam intensity at the depth of the dopant atom is significant.

By identifying the important Bloch wave transitions it is possible to optimize HAADF experiments on dopant atoms. Consider for example HAADF imaging of substitutional atoms. If scattering were restricted to the intraband transition of the 1*s* state, the HAADF dopant atom contrast would have the desirable property of being independent of the depth of the dopant atom (neglecting absorption effects). Non-1*s* states are undesirable since they are interband scattered to the 1*s* state, thereby giving rise to variations in the high-angle scattering with dopant atom depth. Since a large objective aperture increases the contribution of the non-1*s* states to the probe intensity (Peng *et al.*, 2004), the ideal size of the aperture is that which is just sufficient to attain good resolution of the atom columns. For optical sectioning experiments on substitutional atoms two criteria must be satisfied. First the

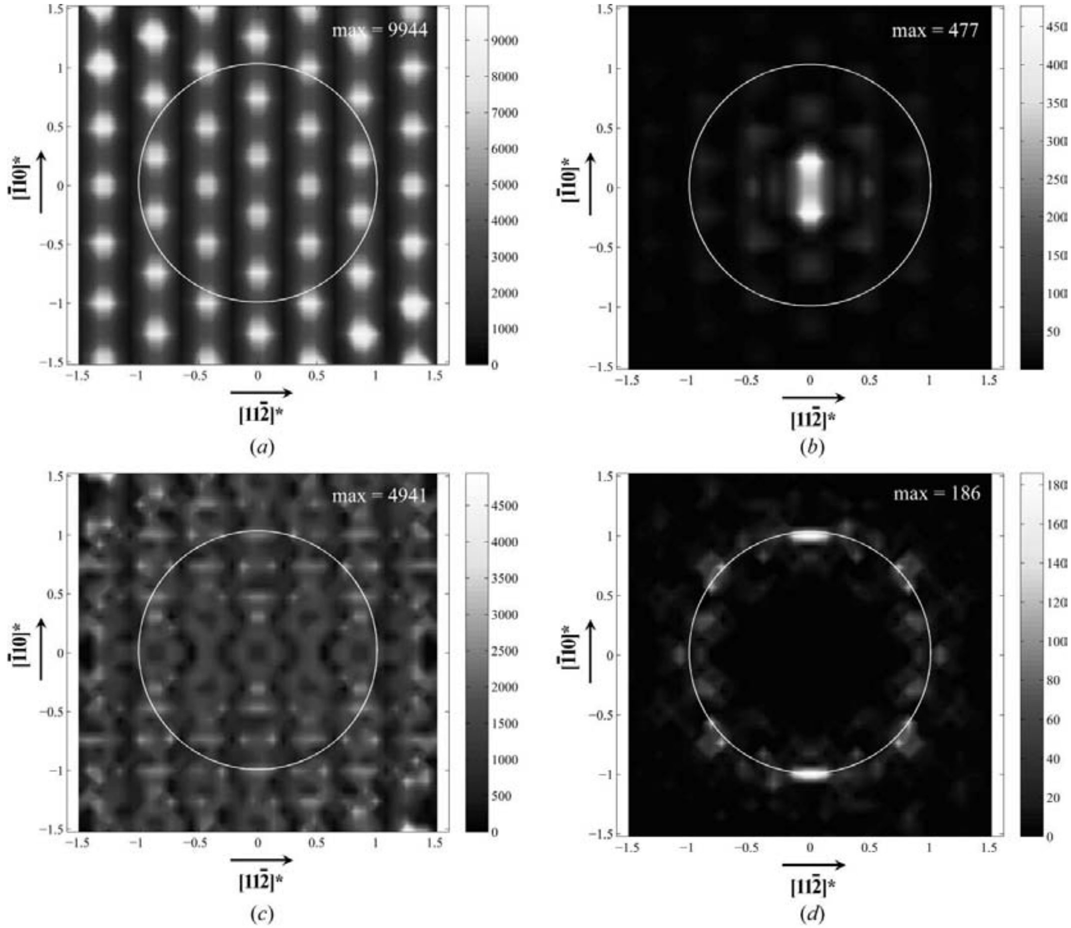

Figure 13
(a)–(d) are $I^{4,4}$, $S^{4,4}$, $I^{17,4}$ and $S^{17,4}$ plots for an interstitial W atom in [111]-Fe. The horizontal and vertical axes represent the component of $\mathbf{k}_t$ along the [11$\bar{2}$]* and [$\bar{1}$10]* reciprocal-lattice vectors, respectively ($\mathbf{k}_t$ is in Å^{-1} and the half width of the image corresponds to 30 mrad at 300 kV). The boundary of a 20 mrad STEM objective aperture is indicated by the open circle. In each figure the maximum value is indicated in the top right-hand corner.

STEM probe must consist of largely the 1s Bloch state when it is focused at the dopant atom depth. Secondly, when the probe is focused slightly away from the dopant atom the electron wavefunction at the dopant atom depth must have a negligible contribution from the 1s state. This would minimize any high-angle TDS scattering of the defocused probe by the dopant atom, thereby resulting in atoms that are less elongated along the foil thickness direction. A more detailed study of the optimum conditions for HAADF dopant atom imaging will be presented in a separate paper.

References

Allen, J. E., Hemesath, E. R., Perea, D. E., Lensch-Falk, J. L., Li, Z. Y., Yin, F., Gass, M. H., Wang, P., Bleloch, A. L., Palmer, R. E. & Lauhon, L. J. (2008). *Nat. Nanotechnol.* **3**, 168–173.

Benthem, K. van, Lupini, A. R., Kim, M., Baik, H. S., Doh, S. J., Lee, J.-H., Oxley, M. P., Findlay, S. D., Allen, L. J. & Pennycook, S. J. (2005). *Appl. Phys. Lett.* **87**, 034104.

Bird, D. M. & King, Q. A. (1990). *Acta Cryst.* A**46**, 202–208.

Buxton, B. F., Loveluck, J. E. & Steeds, J. W. (1978). *Philos. Mag. A*, **38**, 259–278.

Cosgriff, E. C. & Nellist, P. D. (2007). *Ultramicroscopy*, **107**, 626–634.

Cowley, J. M. & Moodie, A. F. (1957). *Acta Cryst.* **10**, 609–619.

Fertig, J. & Rose, H. (1981). *Optik*, **59**, 407–429.

Gao, H. X. & Peng, L.-M. (1999). *Acta Cryst.* A**55**, 926–932.

Hall, C. R. & Hirsch, P. B. (1964). *Proc. R. Soc. A*, **286**, 158–177.

Hirsch, P. B., Howie, A., Nicholson, R. B., Pashley, D. W. & Whelan, M. J. (1965). *Electron Microscopy of Thin Crystals.* Washington: Butterworths.

Kirkland, E. J. (1998). *Advanced Computing in Electron Microscopy.* New York: Plenum Press.

Loane, R. F., Kirkland, E. J. & Silcox, J. (1988). *Acta Cryst.* A**44**, 912–927.

Mendis, B. G. (2008). *Acta Cryst.* A**64**, 613–624.

Mendis, B. G. & Hemker, K. J. (2008). *Ultramicroscopy*, **108**, 855–864.

Nellist, P. D. & Pennycook, S. J. (1996). *Science*, **274**, 413–415.

Nellist, P. D. & Pennycook, S. J. (1999). *Ultramicroscopy*, **78**, 111–124.

Peng, Y., Nellist, P. D. & Pennycook, S. J. (2004). *J. Electron Microsc.* **53**, 257–266.

Pennycook, S. J. & Jesson, D. E. (1991). *Ultramicroscopy*, **37**, 14–38.

Shannon, M. D., Lok, C. M. & Casci, J. L. (2007). *J. Catal.* **249**, 41–51.

Voyles, P. M., Grazul, J. L. & Muller, D. A. (2003). *Ultramicroscopy*, **96**, 251–273.

Voyles, P. M., Muller, D. A., Grazul, J. L., Citrin, P. H. & Gossmann, H.-J. L. (2002). *Nature* (*London*), **416**, 826–829.

Voyles, P. M., Muller, D. A. & Kirkland, E. J. (2004). *Microsc. Microanal.* **10**, 291–300.